Capillary Levelling of a Liquid Step on a Floating Solid Film

CAPILLARY LEVELLING OF A LIQUID STEP ON A FLOATING SOLID FILM

BY

LAUREN DUTCHER, B.Sc.

A Thesis

Submitted to the Department of Physics and Astronomy

and the School of Graduate Studies

of McMaster University

in Partial Fulfilment of the Requirements

for the Degree of

Master of Science

©Copyright by Lauren Dutcher, December 2021

All Rights Reserved

Master of Science (2021) McMaster University

(Physics and Astronomy) Hamilton, Ontario, Canada

TITLE: Capillary levelling of a liquid step on a floating solid film

AUTHOR: Lauren Dutcher

B.Sc., (Physics)

University of Guelph, Guelph, Canada

SUPERVISOR: Dr. Kari Dalnoki-Veress

NUMBER OF PAGES: xii, 53

Abstract

This thesis outlines the research I completed during my M.Sc. work. This research focuses on analyzing the deformations of an elastic film at an imposed boundary. Specifically, I prepared a trilayer thin film sample geometry where a glassy polymer thin film floats atop a liquid layer and a final liquid layer sits on the top and partially covers the films below.

This thesis is organized into four chapters. The first chapter details main topics associated with the background knowledge necessary for understanding the results. This introductory chapter provides an overview of the polymers that create the thin films, fluid dynamics associated with the flow of these polymer films in their liquid state and capillarity, as the length scales and forces involved in the experiments are at a length scale where gravity can be neglected. The second chapter discusses the experimental design involving sample preparation and explanations of the techniques used for data collection. The third chapter presents the results of the experiments and discusses our understanding of these results. The fourth chapter concludes the thesis.

Acknowledgements

I don't know where to begin as I am so thankful to so many. Kari: you are truly the most supportive supervisor and your positivity and love of research is inspiring to be near. You have completely changed my perspective on my project, from disappointed to excited, countless times with a 5 min meeting. Carmen, my secondary supervisor: thank you for not only being a friend and real human contact during a time of lockdowns and zoom meetings but also for your wisdom and guidance throughout this degree. To my labmates: Johnathan, Hamza, Adam, JC, Yasmin, John, Angela and Julia: it has been so fun to work with you all. I am so lucky to continue to learn from this group in the next 4 years. To my dad: thank you for teaching me your love of physics, there is no way I would be here without you. To my mom: thank you for supporting me in everything that I choose. To Hayden: thank you for believing in me more than I believe in myself. I love you. (Also thank you for having the two cutest dogs, who's stress relieving abilities are unmatched.) To my family and friends: thanks for cheering me on the whole way through.

Contents

List of Figures

Chapter 1

Introduction

Surface tension is a phenomena seen everywhere. Because of the attraction between molecules in a liquid, along with a liquid's ability to flow, many interesting phenomena arise. Water striders can walk across the surface of a pond, a jet of tap water breaks up into droplets, soap bubbles form perfect spheres and the rain from a storm rolls off your tent as you stay dry inside. Our understanding of surface tension is essential to developing new technologies to benefit our everyday life.

As a droplet of water sitting atop a solid substrate increases in volume, the shape of this droplet will transition from a spherical cap to a flat puddle due to the force of gravity. The angle at which the puddle contacts the substrate is defined by a balance in interfacial tensions associated with the solid, liquid and vapour phases. This force balance is true for a liquid on top of a solid substrate or a liquid atop an immiscible liquid, although the substrate dramatically effects the equilibrium shape [1,2]. In this thesis, thin polymer films are used to probe, what happens to a thin flexible solid sheet floating atop a liquid at a liquid boundary. This system corresponds to an intermediate system between the two well characterized cases: a liquid on a solid and a liquid on a liquid.

Polymers are everywhere, making up the soles of our shoes, the tires we

drive on, to novel drug delivery technologies [3]. Polymers can be synthetically made, but are also found naturally, like DNA. One useful feature of polymers is that their properties are tunable with temperature. Of interest to the experiments detailed in this thesis, the polymers which are solid, elastic materials at room temperature transition into flowing fluids above a critical temperature. In addition, the viscosity decreases with an increase in temperature allowing for customization of experimental timescale. The experiments detailed in chapter 2 harness these temperature dependent polymer properties.

In this thesis, polymers were prepared into thin films. Polymer thin films, with thicknesses $\sim$ 10 - 100 nm while the lateral scale is on the order of micrometers to centimeters, are an ideal geometry for various reasons. The first reason is that the force of gravity can be neglected due to the negligable mass associated with the thickness of the films. The second reason involves these films in their liquid state. For thin liquid films, the boundary effects associated with the flow profiles dominate the entire thickness of the films, this signifies a different regime than bulk fluids. Lastly, these liquid thin films have many real life applications including biological membranes or engineered paint and adhesives [4]. Understanding the boundary effects is important as technologies that utilize thin polymeric coatings get smaller [5–7].

The experiments associated with this thesis involve stacked thin polymer films. The bottom film is heated until it becomes a liquid and a second solid polymer thin film rests above it. A third liquid thin film partially covers the solid film creating a boundary condition not yet studied in literature. This thesis is organized into four chapters. Chapter 1 outlines theory regarding polymers and their characteristics, fluid dynamics and the simplifications associated with liquid thin films, surface tension, Laplace pressure and capillarity. In the second chapter, the experimental details associated with the work completed are discussed. Chapter 3 contains the analysis and results obtained. Finally, Chapter 4 draws conclusions.

1.1 Polymers

Polymers are macromolecules with repeating monomer units covalently bonded together. The number of monomer units within a polymer molecule is referred to as the degree of polymerization and this relates to the length of the polymer chain. Although the length of the polymer is an important quantity, this information is usually given as the molecular weight. Since it is very difficult to synthetically manufacture polymers that are completely monodisperse, most solutions include a measurement of an average polymer length. The molecular weight is defined in two ways: the number average molecular weight and the mass average molecular weight. The number average molecular weight is given by:

$$M_n = \frac{\sum_i N_i M_i}{\sum_i N_i} = \sum_i n_i M_i, \tag{1.1}$$

where N_i is the number of molecules with mass M_i and n_i is the fraction of molecules with mass M_i. The weight-average molecular weight is given by

$$M_w = \frac{\sum_i W_i M_i}{\sum_i W_i} = \sum_i w_i M_i, \tag{1.2}$$

where W_i is the mass of molecules with molar mass M_i and w_i is the mass fraction of molecules with mass M_i. The weight-average molecular weight M_w gives more emphasis to the larger polymer chains in the distribution and therefore $M_w \geq M_n$. The polydispersity index (PDI) is a measurement of the distribution of polymer molecules within a sample; it is calculated by the ratio of weight average molecular weight over the number average molecular weight:

$$\text{PDI} = \frac{M_w}{M_n}. \tag{1.3}$$

A PDI value of 1 corresponds to a completely monodisperse sample while a PDI > 1 corresponds to a polydisperse sample [8].

These assembled monomer units that form polymer chains can take on a

multitude of conformations due to the flexibility of the covalent bonds. The flexibility of polymer chains is also dependent on the polymer architecture. Various types of polymers exist including: linear, ring, branched, ladder and dendrimer to name a few [8]. The architecture of interest in this thesis is the simple linear polymers, meaning the monomers form a long string-like molecule as shown in Figure 1.1. These linear chains can become entangled together, especially as the molecules become long - large M_w. The entanglement molecular weight is another important characteristic of polymers, where below this value the chains are short and relatively free and above this value the chains become an entangled network. The chemical structure shown in Figure 1.1(a) shows the monomer for the common polymer polystyrene, used in this thesis, which has alternating phenol groups off a long hydrocarbon backbone. Polystyrene has an entanglement molecular weight of 19100 g/mol [9]. Figure 1.1(b) shows the monomer units of the polymer polysulfone, the second polymer used in this thesis.

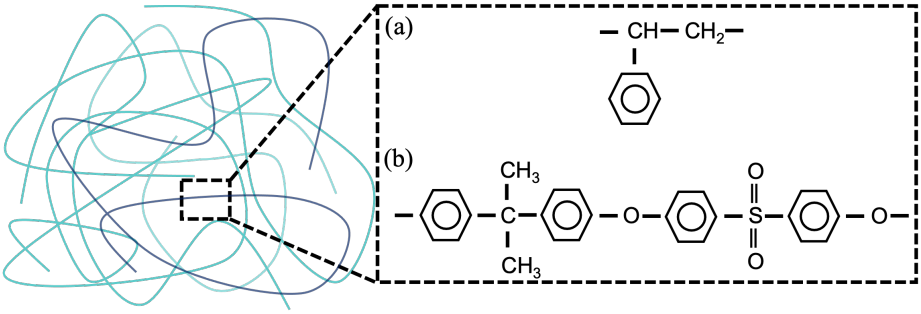

Figure 1.1: Linear polymer chain entangled into a network. (a) Styrene monomer for the polymer polystyrene. (b) Monomer for the polymer polysulfone.

1.1.1 Viscoelasticity

Generally, polymer melts form solids upon cooling from a melt state. Solids are materials that, when acted upon by a shear stress, maintain their structure. An ideal example, called a Hookean solid, can aid in understanding a solid's

stress response. A Hookean solid temporarily moves out of it's equilibrium configuration when acted upon by a shear stress, it then acts elastically to return to its original shape. This intermediate configuration is shown in Figure 1.2 where a shear stress is applied towards the right and the solid shifts in response. Here the shear stress, σ, is given by $\sigma = F/A$, where F is the applied force and A is the area over which the force is acting. The material's reaction to this applied force is to produce a strain, e. This strain is given by $e = \Delta x/y$, where Δx and y are defined in Figure 1.2. The Hookean solid, just like a Hookean spring, acts linearly with response to the force and the corresponding proportionality constant referred to as the modulus is given by $G = \sigma/e$ [10].

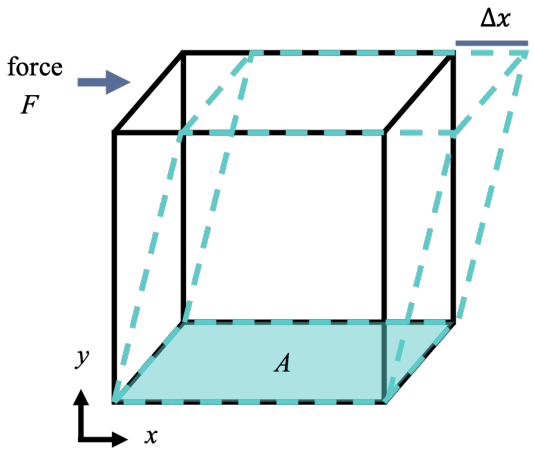

Figure 1.2: Hookean solid (solid line) and its distortion to a force, F, acting to the right (dotted line).

In contrast to solids, we can look at an ideal liquid: a Newtonian liquid. For a liquid, the application of a shear stress results in a strain that is time-dependent. For example, if a liquid is sandwiched between two parallel plates, as shown in Figure 1.3, with one plate moving at velocity, v, then the force that opposes the motion of these plates is given by $F = A\eta v/y$. Here A is the area of the plates, y is the distance between the plates and η is a coefficient

called viscosity which is the fluid's resistance to any deformation. Since the term v/y is the definition of the strain rate, $\dot{e}$, we can more generally define $\sigma = \eta\dot{e}$. Viscosity follows the thermally dependent behaviour characterized by the Arrhenius equation [10]:

$$\eta = \frac{G_0}{\nu} e^{\frac{\epsilon}{kT}}, \tag{1.4}$$

where ν is the frequency of molecular vibrations, ϵ is the activation energy, and k is the Boltzmann constant. This equation shows that with an increase in temperature the viscosity decreases [10]. Polymer melts flow and behave like Newtonian liquids.

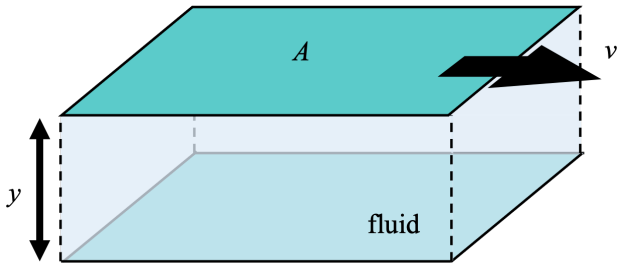

Figure 1.3: Schematic of Newtonian liquid sandwiched between two parallel plates of area, A, moving with velocity, v, with a distance y between them.

Perhaps the most interesting behaviour of polymers is that they display both a solid-like response and a liquid-like response that depends on the timescale of the system. This timescale-dependent phenomena defines viscoelasticity. When a constant force acts on a polymer material, on a short timescale, this object will react elastically as a solid. If this force persists to long timescales, the polymer material will flow with a viscosity as a liquid. Figure 1.4 shows this viscoelastic relationship where G_0 is an instantaneous shear modulus. The timescale at which the object changes from solid-like behaviour to liquid-like behaviour is defined by the relaxation time, τ, as labelled in Figure 1.4 [10].

There is a general equivalence in the viscosity between time and temperature

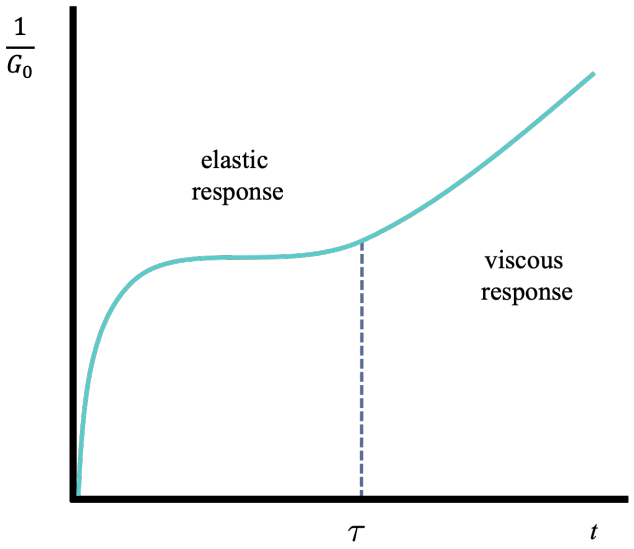

Figure 1.4: Shear strain, $1/G_0$, versus time, t, plot with characteristic elastic response time, τ, marked.

and consequently, a shift factor, a_{T}, can be defined:

$$a_{\mathrm{T}} = \frac{\eta(T)}{\eta(T_0)} = \frac{\tau(T)}{\tau(T_0)}, \tag{1.5}$$

where T_0 is a reference temperature and T is the temperature of the experiment. An empirical law was found that describes the temperature dependence of the viscosity:

$$\eta(T) = \eta_0 \exp\left(\frac{T_A}{T - T_v}\right), \tag{1.6}$$

where T_A is the activation temperature and T_v is the Vogel temperature. Equation 1.6 is called the Vogel-Fulcher law. An equivalent form of this empirical law is called the WLF equation, named after Williams, Landel and Ferry, and states:

$$\log a_T = \frac{-C_1(T - T_0)}{C_2 + (T - T_0)}, \tag{1.7}$$

where C_1 and C_2 are quasi-universal constants for polymers at 17.4 and 51.6 K,

respectively [10].

1.1.2 Glass Transition

Most polymers form glasses, meaning at low temperatures they behave like solids with a finite shear modulus, but at high temperatures they are liquids that flow with a temperature dependant viscosity. Glasses are different from regular solids in that they show a disordered molecular state similar to a liquid, whereas typical solids have a characteristic long-range molecular order. The temperature at which this transition from solid-like properties to flowing in a melt state with a relaxation time accessible at an experimental timescale is defined as the glass transition temperature T_{g}. At T_{g} there is a discontinuity in certain thermodynamic quantities. For example, the volume of a polymer melt as it is cooled will follow one of two distinct pathways as shown in Figure 1.5. The first, marked crystal, shows a sudden decrease in the volume at a temperature T_{m} referring to a transition into a crystalline state. This sharp volumetric decrease is the characteristic behaviour of a first-order phase transition [10]. The other pathways marked glass 1 and glass 2, show a sudden slope change at T_{g} marking the transition from solid to glass. The exact T_{g} value depends on the rate of cooling [10]. The T_{g} values of the two types of polymers used in this work are 373 K (100 °C) and 459 K (186 °C) for polystyrene and polysulfone, respectively [9].

As seen in Figure 1.5, the volume of an object will increase as the temperature is increased. The expansion of materials is due to the interactions and forces between molecules in the material and will occur for gases, liquids and solids [11]. To a first order approximation, the force between molecules in a solid can be represented by a spring force, F, described by Hooke's law: $F = -kx$, where k is the spring constant and x is the separation between molecules. Including higher order terms, that account for mutual repulsion of molecules and a vibrational term, the potential between molecules includes a cubic and quartic

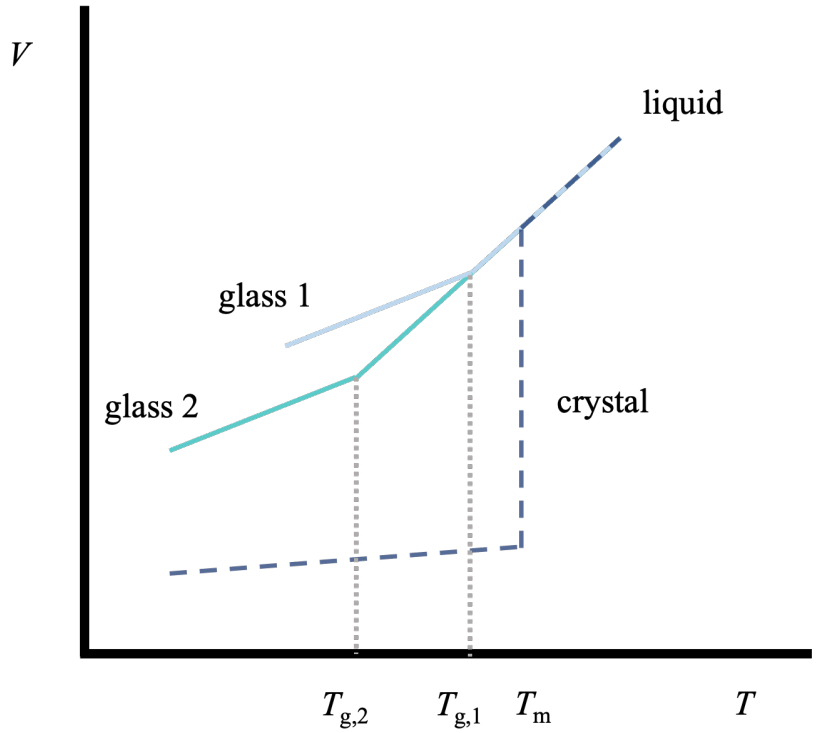

Figure 1.5: Volume, V, versus temperature, T, plot showing a glass forming liquid's transition to a glass (solid lines) and a crystal (dashed line). The two glasses refer to different cooling rates where glass 2 is cooled faster than glass 1.

term. The cubic repulsive term accounts for an increase in average molecular spacing within the solid [11]. This expansion occurs in all three dimensions and is characterized by a thermal expansion coefficient defined as:

$$\alpha \equiv \frac{1}{V}\left(\frac{\Delta V}{\Delta T}\right)_p, \tag{1.8}$$

where V is the volume of the solid and T is the temperature. This coefficient refers to the change in volume with a change in temperature at a given constant pressure, p. The consequences of this material expansion are vast, for example it is the working principle behind mercury thermometers [12]. The volume thermal expansion coefficients for materials involved in this thesis are: polystyrene: 1.7−

2.6×10^{-4} K^{-1} [9], polysulfone: 2.16×10^{-4} K^{-1} [13] and silicon: $\sim 9 \times 10^{-6}$ K^{-1} [14]. Thermal expansion can introduce wrinkling in the thin films involved in this thesis.

1.1.3 Wrinkling

Wrinkling occurs in systems with a hard outer crust atop a soft inner layer when a compressive force acts in-plane as shown in Figure 1.6(a). This force introduces a stress to the system and the system releases this stress by forming out-of-plane wrinkles as shown in Figure 1.6(b) with a characteristic wavelength, λ.

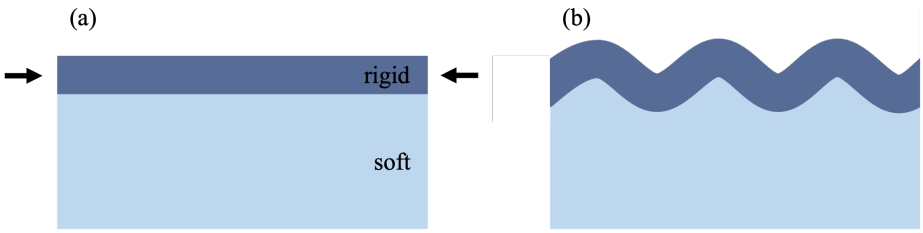

Figure 1.6: Schematic of a soft layer under a rigid crust. (a) A compressive force acts on the rigid layer, shown with arrows. (b) The system releases the stress by creating wrinkles.

Wrinkling in systems with a hard outer crust atop a soft inner layer have been studied. The mechanism to induce a compressive force varies between studies. Chemical swelling is one way to introduce compression [15–17]. Another way is to apply a pre-strain to the system, which upon release, introduces compression [18–23]. Introducing this force through thermal expansion has also been used before with a PDMS - metal deposition system [24]. In this thesis, we use thermal expansion to induce wrinkling in thin films.

The samples created for the experiments in this thesis involve two thin films stacked atop a silicon substrate as shown in Figure 1.7(a). Geometrically, these thin films have a large length scale in the x-y plane but have a very small variation in the z direction. When looking at the length scale associated with the thickness, the plane of the samples can be viewed as infinite. The polymers

making up the films are specifically chosen so that the bottom film transitions into a liquid at a lower temperature than the top film. The silicon substrate's thermal expansion coefficient is 2 orders of magnitude smaller than the polymer films' thermal expansion coefficients, so it's expansion can be neglected. The edges of the silicon substrate create a constraint to the polymer films' expansion in the x-y plane so now they can only expand in the vertical direction. While both films are heating, but below their T_g values, the films remain glassy solids that have stresses building in the x-y plane, shown in Figure 1.7(b). Finally, these samples are heated above the base film's T_g, but below the top film's T_g so that the top film remains a glassy solid while the base film can flow as a liquid. At this point, the liquid film can flow and the top film wrinkles to relieve the compressive stress, this is shown in Figure 1.7(c).

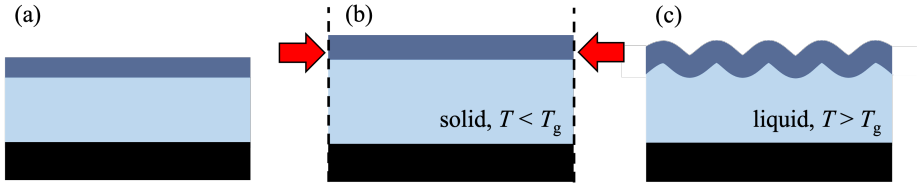

Figure 1.7: Schematic of two stacked polymer films (light and dark blue) atop a silicon substrate (black). (a) A compressive force (red arrows) is introduced to the system due to constraints in the x-y plane. (b) The system wrinkles once it is heated above the glass transition temperature of the inner polymer film.

1.2 Fluid Dynamics

Fluid dynamics is a complex area of physics dealing with the flow of liquids. The movement of liquids is so complex because different elements within a single liquid object behave separately. Although, fundamentally different than a solid, one can draw similarities between these two material phases. Classically, an object's motion is described by Newton's laws, of interest here is Newton's second law which states that if a net force, $\vec{F}$, acts on an object, the object accelerates in proportion to it's mass, m: $\vec{F} = m\vec{a}$. For a liquid, this force

equation can be written in in terms of the density of the liquid, ρ:

$$\vec{F} = \rho \frac{d\vec{v}}{dt}, \tag{1.9}$$

where $\vec{v}$ is a liquid element's velocity. The full form of this equation, taking into account the force of gravity and the opposing viscous dissipation associated with the fluid's movement is given as [25]:

$$\frac{\vec{\partial v}}{\partial t} + (\vec{v} \cdot \nabla)\vec{v} = -\frac{1}{\rho}\nabla p + \nu \nabla^2 \vec{v} + g, \tag{1.10}$$

where $\vec{v}$ is the three dimensional fluid element's velocity, p is the pressure acting on a fluid element, ν is the kinematic viscosity ($\nu = \eta/\rho$), g is the acceleration due to Earth's gravity and the fluid is assumed to be incompressible. Equation 1.10 along with the incompressibility condition: $\nabla \cdot v = 0$, constitute the Navier-Stokes equations [1]. The left side of equation 1.10 constitutes a material derivative which describes the velocity rate of change following the fluid. The material derivative is calculated by a simple chain-rule calculation of the time derivative on the x- y- and z-components of the fluid parcel's velocity - where the velocity depends on position and the position depends on time. Taking a closer look, the first term within this material derivative describes the acceleration of the fluid parcel and the second term is the inertial term. The right-hand side of equation 1.10 introduces the forces involved with the fluid's motion. The first term takes the pressure into account while the second term is the viscous term associated with the internal friction due to the fluid's viscosity. The final term in equation 1.10 accounts for a gravitational body force per unit mass that may be present [25].

The Reynolds number, Re, is an important characteristic to define the type of flow a certain fluid will experience. The Reynolds number is defined as the

ratio of inertial flow to viscous flow:

$$\mathrm{Re} = \frac{\text{inertial term}}{\text{viscous term}} = \frac{(\vec{v}\cdot\nabla)\vec{v}}{\nu\nabla^2\vec{v}}. \tag{1.11}$$

The value of the Reynolds number therefore tells us about the characteristic flow patterns the fluid experiences. The value of Reynolds numbers can be broken up into two cases: Re $>>$ 1 and Re $<$ 1. For Re $>>$ 1, the inertial term dominates over the viscous term, this defines flow with a small viscosity. A consequence of low viscosity is that the flow of the fluid is highly susceptible to small disturbances which will cause turbulent flow. In contrast, a low Reynolds number refers to a fluid where the inertial effects are negligible and viscous effects dominate. An interesting characteristic of low Re fluids is that there is a reversibility associated with the flow. For example, if a dyed blob of high viscosity is sheared between two concentric cylinders, a reversal in the rotation reverts the blob to the initial configuration [25]. The polymer melts with high viscosity and low velocities involved in this thesis correspond to low Re flows.

1.2.1 Thin Film Equation

The Navier-Stokes equations are complicated to solve for. Complications include: it is valid in three-dimensional space - meaning this equation should be broken up into separate $x-, y-, z$-component equations, the inertial term causes a non-linearity and the viscous term makes it a second-order differential equation. Luckily, there is a useful and straightforward simplification to equation 1.10 by use of the lubrication approximation. This approximation is valid for flows that are dominant in one direction and therefore negligible in the perpendicular directions - ideal for thin film situations investigated in this thesis. Another restriction involves the continuity of the flow at the interface between the fluid and the solid substrate. For thin viscous films, where the flow is parallel to the plane of the film, the velocity, $\vec{v}$, must be zero at the substrate interface since the substrate is stationary. The consequence of this continuity is that the

viscous term ($\nu\nabla^2\vec{v}$) now dominates the inertial term ($(\vec{v}\cdot\nabla)\vec{v}$) since the small length scale perpendicular to the substrate means the flow is slow. This flow corresponds to a low Reynold's number. The continuity restriction must also mean there is a gradient in the flow velocity in the direction perpendicular to the flow [1].

Incorporating the lubrication approximation, equation 1.10 becomes:

$$-\nabla p + \eta\nabla^2\vec{v} = 0, \tag{1.12}$$

where η is the viscosity as defined by $\eta = \nu\rho$ and the incompressibility condition $\nabla\cdot\vec{v} = 0$ is still valid [1]. The final step in solving the Navier-Stokes equations involves implementing boundary conditions.

1.2.2 Flow Profiles

Various boundary conditions exist, depending on the geometry of the system. The flow profile is determined by the two interfaces of the liquid. A common flow profile is Poiseuille flow which refers to a velocity profile that is parabolic in shape. One situation which produces Poiseuille flow is where there is no flow at the substrate - liquid interface and a free boundary at the liquid - air interface. Due to the air's extremely low viscosity, there is nothing on the air side of this interface that would counteract the viscous force while ensuring stress is continuous in the system. This condition means the stress, proportional to $\partial\vec{v}/\partial z$, must be zero at the liquid air interface. This flow profile is shown in Figure 1.8(a) [1]. Another profile that results in Poiseuille flow is when both boundaries have a zero flow condition, this is shown in Figure 1.8(b). Both these flow profiles are present in the stacked film configuration outlined in Chapter 2.

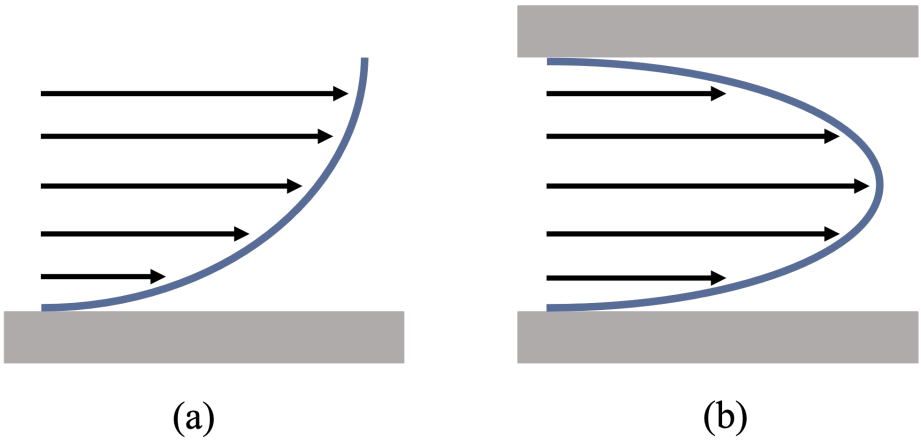

Figure 1.8: Poiseuille flow profiles. (a) Flow profile for a no slip bottom boundary condition and a free top boundary condition. (b) Flow profile for a no slip boundary condition at both interfaces.

1.2.3 Single-Phase Spreading

The wrinkling phenomena described in section 1.1.3 relaxes over time as the underlying fluid flows. This type of relaxation under an elastic sheet can be represented by a Hele-Shaw cell as shown in Figure 1.9. This flow is called single-phase spreading and is described by the continuity equation in Cartesian coordinates:

$$\frac{\partial h}{\partial t} + \frac{\partial}{\partial x} hv = 0, \tag{1.13}$$

where $h(x,t)$ is the height of the fluid enveloped between the elastic sheet and the substrate, x is the flow direction and v is the fluid velocity. The fluid flows due to a pressure gradient exerted by the elastic sheet while gravitational effects can be neglected due to the extremely small height profile. Assuming no stretching and only bending of the elastic sheet, linear elasticity can be invoked which is governed by:

$$p = B\nabla^4 h, \tag{1.14}$$

where B is the bending modulus and p is the pressure. Equation 1.14 arises from calculating the pressure associated with bending a rod [26]. When looking at the wrinkling system in the view shown in Figure 1.9, the elastic sheet can be equated to a bending rod and the perpendicular plane, running the length of the wrinkle, has no bending pressure. This bending-dependent pressure given in equation 1.14 can then be inserted into Darcy's law for fluid velocity [27]:

$$v = -\frac{h^2}{12\mu}\frac{\partial p}{\partial x}, \tag{1.15}$$

where μ is the fluid viscosity. Simplifying equations 1.13 through 1.15 a final equation for the change in the elastic sheet's height as a function of time is obtained:

$$\frac{\partial h}{\partial t} = \frac{B}{12\mu}\frac{\partial}{\partial x}\left(h^3\frac{\partial}{\partial x}\nabla^4 h\right), \tag{1.16}$$

which involves a spatial derivative of order six [28]. Relating this to the wrinkling system outlined in section 1.1.3, the spatial x coordinate in Figure 1.9 relates directly to the wrinkling wavelength, λ. Therefore the relationship between wrinkling wavelength and time becomes:

$$\lambda \propto t^{1/6}. \tag{1.17}$$

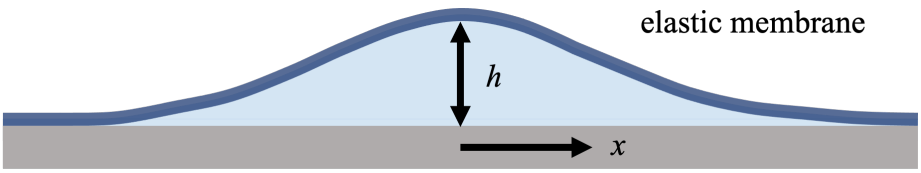

Figure 1.9: Hele-Shaw cell schematic for an elastic sheet over a droplet of liquid.

1.3 Capillarity

When a liquid is left to reach an equilibrium state – whether that be in the vertical walls of a container or free as a puddle resting on a flat surface – the top surface will appear relatively flat. At the molecular level, the liquid is attracted to itself so when a molecule is on the surface, it will have half the attractive interactions as opposed to a molecule in the center of the liquid. This causes a rearrangement to expose the fewest number of molecules at the surface. This molecular rearrangement is the basis of surface tension. Surface tension can be described as the energy cost of interface per unit surface area. Since a perturbation in the surface of a liquid adds surface area, the surface tension will act to reduce this perturbation and minimize the surface area. Surface tension can also be viewed as a force per unit length which is sometimes called the capillary force. Surface minimization due to surface tension manifests itself in many different ways, including a stream of water breaking up into droplets (this is known as the Plateau-Rayleigh instability) or the perfect spherical shape of a soap bubble [1].

1.3.1 Laplace Pressure

When a surface is curved – as it is in the case of spherical droplets for example – the system experiences a pressure difference inside versus outside the curved surface. This pressure difference is called the Laplace pressure. A straight forward example for calculating the pressure difference is to look at increasing the radius, R, of a spherical droplet by the the amount, dR, shown in Figure 1.10. The work done by this displacement can be written as:

$$\delta W = -p_d dV_d - p_e dV_e + \gamma_{de} dA, \tag{1.18}$$

where the first term involving the droplet's pressure, p_d, describes the droplet's increase in volume, the second term involving the environment's pressure, p_e

describes the environment's decrease in volume and the third term involving the interfacial tension, γ_{de}, describes the increase in the droplet's surface area. Mechanical equilibrium states that $\delta W = 0$ therefore the difference in pressures can be described as

$$\Delta p = p_d - p_e = \gamma_{de}\frac{2}{R}. \tag{1.19}$$

As seen by the inverse relationship between the pressure difference and the radius, a droplet with a smaller radius has a greater inside pressure. This simple example can be used to generalize the pressure difference between two fluids as [1]:

$$\Delta p = \gamma\left(\frac{1}{R_1} + \frac{1}{R_2}\right) = \gamma C, \tag{1.20}$$

where R_1 and R_2 are the two radii that define the curvature, C, at a specific point in orthogonal planes. The agreement between equation 1.19 and equation 1.20 is obvious as the two radii of curvature for a spherical droplet are the same and C becomes $2/R$ [1].

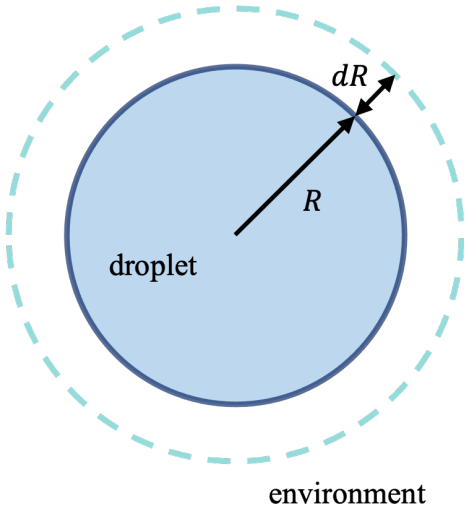

Figure 1.10: Spherical droplet of liquid with radius, R, increasing by dR.

1.3.2 Capillary Length

As discussed earlier, a liquid flows to minimizes it's surface area which results in smooth surfaces that minimize the curvature. This energy minimization must work in conjunction with Laplace pressure to ensure smooth transitions at edges. The length at which edge effects occur is called the capillary length, κ^{-1} and is shown in Figure 1.11. This curvature can be seen at the edges of a filled water glass, which creates a meniscus. The value of this length is found by equating the Laplace pressure γ/κ^{-1} and the hydrostatic pressure $\rho g \kappa^{-1}$. Here the hydrostatic pressure refers to the pressure experienced in a liquid of density, ρ, at a depth, κ^{-1}. Balancing these pressures gives the capillary length [1]:

$$\kappa^{-1} = \sqrt{\frac{\gamma}{\rho g}}. \tag{1.21}$$

At length scales below the capillary length, gravity becomes negligible and surface tension dominates. In contrast, at larger length scales gravity dominates to flatten the liquids surface [1].

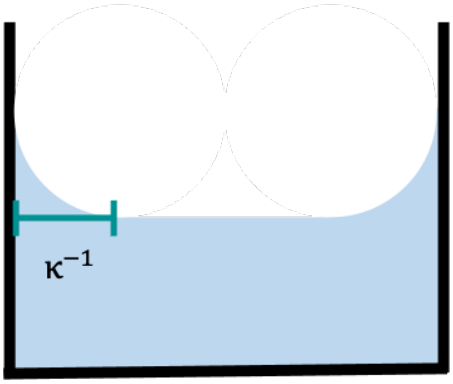

Figure 1.11: Schematic of capillary length, κ^{-1}, in a glass of water.

1.3.3 Wetting

When a liquid is deposited on a solid or liquid substrate, two different regimes form due to the energy of the substrate. A spreading parameter, S, can be defined that compares the energy of the substrate when dry to the energy of the same substrate when wet:

$$S = E^{dry}_{substrate} - E^{wet}_{substrate}. \tag{1.22}$$

When this parameter is positive, the liquid wets the substrate completely. When this parameter is negative, this liquid partially wets the substrate, meaning the liquid beads up into spherical caps with a characteristic contact angle, θ_E, as shown in Figure 1.12 [1].

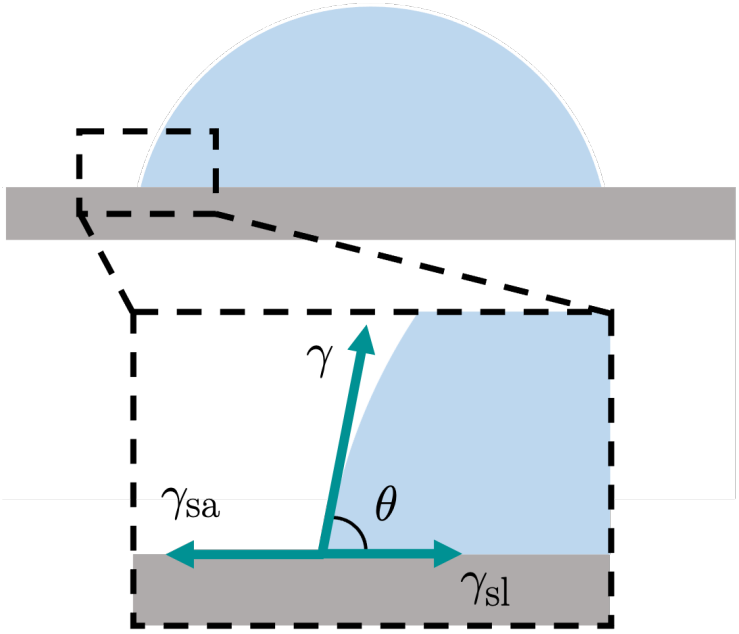

Figure 1.12: Droplet of liquid atop a solid substrate assuming a spherical cap shape. Inset shows the edge of this droplet where interfacial tensions balance.

The contact angle can be defined through the force balance of the interfacial

tensions acting at the edge of the liquid, these forces are outlined in Figure 1.12. On a solid substrate, these forces projected onto the plane of the substrate equate to zero and create Young's relation:

$$\gamma \cos\theta_E = \gamma_{SA} - \gamma_{SL}, \tag{1.23}$$

where γ refers to the liquid-air interface, γ_{SA} refers to the solid-air interfacial tension and γ_{SL} refers to the solid-liquid interfacial tension. Although the vertical force balance appears unbalanced, a solid has such a large modulus that the force is balanced with a very little elastic deformation [1].

This system of a liquid atop a substrate becomes slightly more complex when the solid substrate is replaced with a liquid substrate. In this case, the same three interfacial tensions as before must balance in both the vertical and the horizontal directions, this is known as Neumann's construction. As seen in Figure 1.13, all three capillary forces have a horizontal and vertical component here [1].

1.3.4 Capillary Levelling of a Step

For thin viscous films, like the ones used in this thesis, viscous dissipation and surface energy dominate over inertial and gravitational effects. These systems are ideal for studying capillary forces. For the experiments detailed in chapter 2, a stepped boundary condition is imposed. This initial geometry associated with having a sharp Heaviside step function as a film thickness profile means there is a large excess surface area as compared to a flat film. The sharp height profile equates to a high Laplace pressure due to the small radius of curvature. The Laplace pressure drives flow to smooth out the step – creating less curvature – and therefore a lower energy surface. As discussed earlier, the lowest surface energy is a flat surface (no curvature) and a liquid will flow to obtain this. The flow associated with this levelling is mediated by the viscosity of the fluid.

Capillary levelling with several initial configurations has been studied pre-

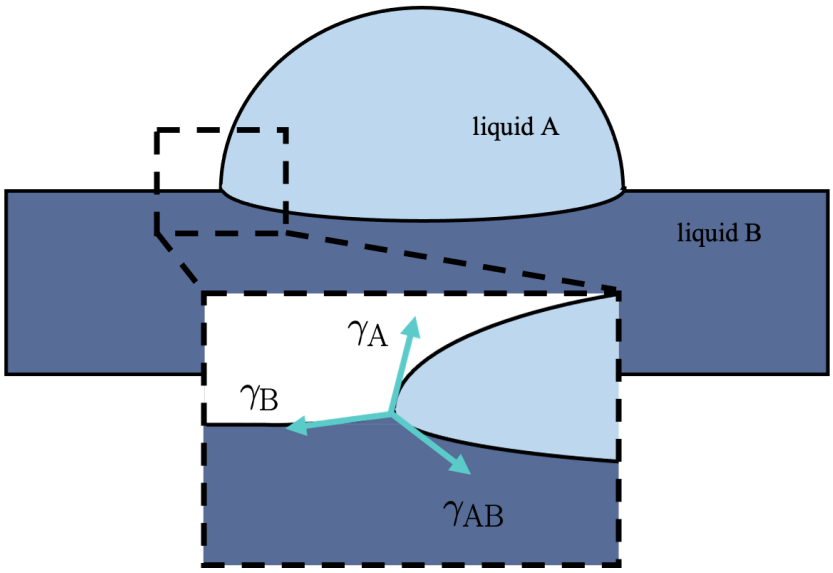

Figure 1.13: Schematic of a liquid droplet atop a liquid substrate. Interfacial tensions balance according to Neumann's construction.

viously [2, 29–36]. Specifically, stepped profiles atop rigid substrates found self-similar profiles where the width of the step increased with time according to a $t^{1/4}$ power law. McGraw *et al.* [31] describes a simplified version of calculations made by Stillwagon and Larson [37]. Assuming the lubrication approximation described in section 1.2.1 is valid for an incompressible fluid, Equation 1.12 gives the 1D flow. This approximation along with a Poiseuille flow profile are valid for the system discussed in [31] as well as in the system discussed in this thesis. A Poiseuille flow profile has a quadratic height dependence so the volumetric flow rate, Q follows as: $Q = -h^3 \partial p / 3\eta$, where ∂ represents a spatial derivative of the pressure, p. The pressure defined as the product of surface tension, γ and the curvature $\partial^2 h$, where again, the derivative is with respect to x [31]. Substituting the pressure along with the mass balance: $\partial h/\partial t = -\partial Q/\partial x$ gives the equation:

$$\frac{\partial h}{\partial t} = \frac{\gamma}{3\eta} \frac{\partial}{\partial x} \left(h^3 \frac{\partial^3 h}{\partial x^3} \right) \tag{1.24}$$

[31, 37]. Equation 1.24 involves a spatial derivative of order 4 on the right side and a single time derivative on the left side. The width of the step, w, is defined in the same spatial coordinate as x and the relationship of $w \propto t^{1/4}$ is obtained [31].

In addition to the growth of the step width, a characteristic bump and dip are present at the high and low side of the step, respectively. These rounded features are understood by material accumulating on the high side of the step as flow travels from high to low pressure [31]. A different study analyzed the effects of an elastic substrate below a stepped polymeric film which found a different scaling of the step width with time. This study showed a $t^{-1/6}$ power law [2]. Other geometries have been studied as well including trenches [34], holes [32] and freestanding films [36].

In the experiments outlined in Chapter 2, the system is made up of layered polymer thin films. A stepped boundary condition is implemented and this stepped film is heated above it's T_{g} value so that it flows. An elastic sheet under the flowing step bends to accommodate the forces present. Capillary forces drive flow to minimize the surface area and the dynamics of this system are analyzed.

Chapter 2

Experimental Details

This chapter outlines the experimental details associated with the research completed for this thesis. Specifically, the preparation of polymer thin films, the stacking of these films to create the ideal sample geometry, as well as the data collection using atomic force microscopy. The sample final sample geometry is shown in Figure 2.1 where the base film, that sits atop a silicon substrate, and the top stepped film are polystyrene films. The middle layer is a polysulfone film. For experiments, the films are heated above the glass transition temperature of polystyrene, but below the glass transition temperature of polysulfone so that the bottom and top films are liquid while the middle layer remains a glassy solid. The experiments conducted were prepared in a laminar flow cabinet to ensure the samples were produced in a clean environment.

2.1 Substrate Preparation

Thin polymer films were prepared by spincoating a polymer solution onto a clean, atomically flat substrate. The first step involves cleaving Silicon (Si) wafers and mica sheets. Silicon wafers are used as the substrate to layer the thin films on. The cleaving process for Si involves placing the 10 cm Si disk,

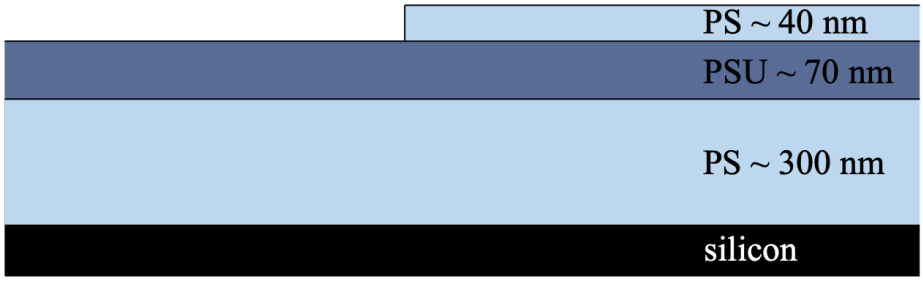

Figure 2.1: Final sample geometry of the stacked thin films. The PS step profile resembles a Heaviside step function prior to heating.

with a native oxide layer, face down on a lens tissue. Then, using a diamond scribe, lines are scored onto the back of the Si disk forming a grid of 1 cm x 1 cm squares that align with the silicon's crystalline structure. Next, a thin metal rod, placed under the lens tissue is used to break the Si disk along these scribed lines by applying pressure on either side. Once the 1 cm x 1 cm Si substrates are carefully removed from the lens tissue, a jet of nitrogen gas is used to remove particles from the substrate. The second substrate used throughout these experiments is 1" x 1" sheets of mica. Similar to Si, mica is a material that has a crystalline structure that allows for cleaving along the crystal planes. Here a sharp scalpel blade is inserted through the center of a sheet of mica and both sheets are pulled apart with tweezers. Cleaving the mica ensures the inside faces of these two mica sheets are flat and again, nitrogen gas is used to remove contaminating particles.

2.2 Solution Preparation

The next step involves preparing polymer solutions to put on the substrates. Two different polymers were used in the experiments outlined in this thesis, polystyrene (PS) with a molecular weight of 17 kg/mol (Scientific Polymer Products, Inc, PDI = 1.05) and polysulfone (PSU) with a molecular weight of 22 kg/mol (Sigma-Aldrich). PS was dissolved in a toluene solvent at varying con-

centrations ranging from 0.5% to 8% weight/weight. The solvent was filtered through a 0.20 µm syringe filter before being added to the polystyrene powder. These solutions were left to dissolve for at least 24 h before being filtered again with a 0.20 µm syringe filter. Polysulfone solutions were created with an identical sample preparation procedure as the polystyrene solutions except for the solvent and concentrations. These solutions were prepared with the solvent cyclohexanone at a concentration of 2% and 4% weight/weight.

2.3 Spin Coating

The PS and PSU solutions were cast into films using a spin coating technique. This technique involves placing drops of the polymer solution onto the substrate of choice and rotating the substrate at high speeds. Throughout the rotation, centrifugal forces push the droplet from the center of the substrate to the outside edges, resulting in a film of uniform thickness. At the same time, the volatile solvents evaporate, leaving behind a thin film of polymer. The PS solutions intended to create the base layer ranged in concentration from 4% to 8% and were spun onto 1 cm x 1 cm silicon substrates. The PS solutions intended to create the topmost step of the sample had a concentration of 0.5% and were spun onto 1" x 1" mica substrates so that they could be easily removed for final sample stacking. The PSU solutions were spun onto the same mica substrates. The substrate with the PS solutions were spun at an acceleration of 5000 rpm/s to a final speed of 4500 rpm for 20.0 s. The PSU solutions were spun at an acceleration of 2500 rpm/s to a final speed of 3500 rpm for 60.0 s. Following the spinning procedure, the PS and PSU films were annealed above their glass transition temperatures at 120 °C and 200 °C, respectively on a Linkam heating stage. The annealing step ensures the polymer chains are relaxed and any remaining solvent has evaporated.

2.4 Floating and Stacking Films

To achieve the desired final configuration, outlined in Figure 2.1, the films must be stacked on top of one another. Specifically, a PSU film is placed atop a PS film spun directly onto an Si substrate. Then a second, thinner, PS film is placed atop the bilayer system. To do this, the second and third films must be removed from their initial mica substrates which is done through a floating process. This process involves scoring the outside edge of a film with a scalpel blade to create and clean edge and then lowering this film covered mica substrate into a high performance liquid chromatography (HPLC) grade ultrapure water bath at an angle, as shown in Figure 2.2. Due to the mica's hydrophilic surface, the water wets the mica substrate. Essentially, the mica substrate prefers the water interface over the film interface therefore the water creates a gap between the film and the mica and the film floats to the surface of the water bath. Surface tension ensures the film remains isotropically taut on the surface.

The reverse process is used to place this floating film onto the final substrate. First, the Si wafer, topped with a PS film, is pulled up through the surface of the water directly underneath the floating PSU film so that the PSU drapes across the sample. The next step is to heat this film above 100 °C - T_g of PS. If wrinkling is desired the sample preparation stops at this point. If further film stacking involving the imposed boundary condition is desired then the films are heated above the temperature at which the system wrinkles to relax any stresses imparted during the floating process and also to eliminate the wrinkling morphology. The samples are heated on a Linkam heating stage to 170 °C to accomplish this. To complete the film stacking, the partial stepped film is floated on top of the PSU film using an identical process to the PSU floating process. The only difference here is that the final PS film is below the entanglement molecular weight and thin enough that the film spontaneously ruptures into several pieces upon agitation on the water surface during the floating process. The rupturing of the films means the edge of these films is a

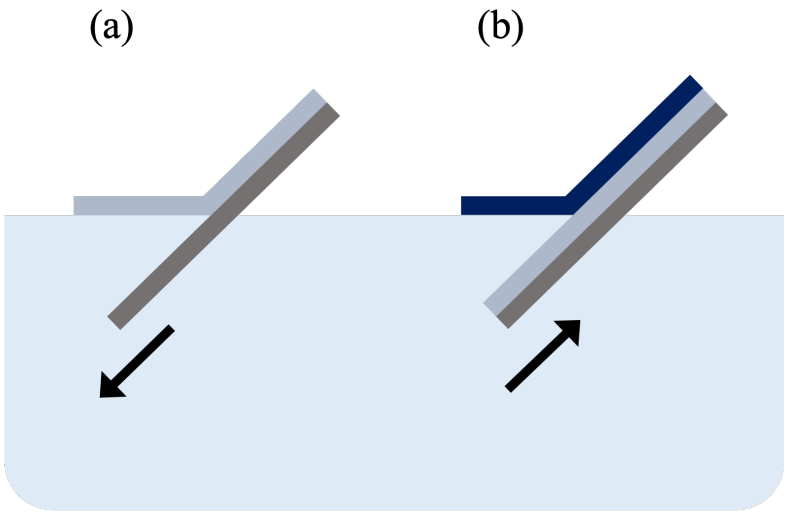

Figure 2.2: Schematic of floating procedure. (a) A polymer film floating off a mica substrate onto the water bath as the sample is drawn down through the water. (b) A polymer film being picked up by a polymer covered Si substrate for stacking.

sharp edge, replicating the profile of a Heaviside step function, and can then be floated onto the sample to produce the boundary condition of interest.

The final samples are then heated in steps on the Linkam heating stage for times ranging from 30 s to 5 min and atomic force microscopy is performed at designated time points.

2.5 Optical Microscopy

Optical microscopy was used throughout sample preparation to view the samples at each step of the process. An Olympus BX51 microscope with 5x, 10x and 20x objectives was used along with a QIMAGING 8-bit CCD camera. At times when contrast between different heights was low, a laser line red-light filter was added to enhance contrast via optical interference fringes.

2.6 Ellipsometry

Ellipsometry is an optical technique used to measure thin films thickness and refractive index [38]. The basic principle is to exploit the optical properties of the phase change associated with light reflected off the top surface of the film and the light reflected off the substrate below the film. Specifically, measurements in this thesis utilized nulling ellipsometry (EP3, Accurion). Three components are necessary to conduct nulling ellipsometry; they are: a linear polarizer and a quarter wave plate before the light reflects off the sample and another polarizer for the reflected light. When elliptically polarized light – light that has components in the x and y direction have different amplitudes and phases – passes through a linear polarizer, linearly polarized light will be reflected off the sample. Essentially, the polarizer acts to suppress electromagnetic waves in a specific direction according to the angle at which the polarizer is oriented. The light passes from the linear polarizer into a quarter wave plate. This component shifts the phase of the light in the plane of incidence by 90 °. Once the light reflects off the two interfaces of the thin film it passes through the second polarizer, sometimes termed the analyzer. By rotating the polarizer and the quarter wave plate, the intensity of the final light passing out of the analyzer can be completely suppressed, hence the name nulling ellipsometry. The thickness of the film can be found through a suitable model, knowing the state of polarization of the optical components [38].

2.7 Atomic Force Microscopy

Atomic force microscopy (AFM) is a sensitive imaging technique used to measure the topology of a sample down to the nanoscale. The basic principle involves a probe, made up of a flexible cantilever and a sharp tip at the end of this cantilever. This probe interacts with the surface of the sample differently depending on the mode of the AFM. For the purposes of this experiment, the

probe oscillates up and down which is known as tapping mode. There is an interaction force between the tip and the surface which causes a deflection of the cantilever. This force is dictated by a Lennard-Jones potential as shown in Figure 2.3 which includes a repulsive force at short length scales 2.3(a), an attractive regime at intermediate length scales 2.3(b) and no force and therefore no deflection of the cantilever at long length scales 2.3(c). A laser aimed at the end of this reflective cantilever is reflected towards a position-sensitive detector. As the topology of the surfaces changes the cantilever and deflection of the cantilever is measured by changes in the reflected laser beam. A piezo-electric material attaches the cantilever to the rest of the AFM. By applying a voltage to this piezo, the material expands and contracts allowing movement across the sample to collect the height profiles. A 3-dimensional reconstruction of the surface is assembled as the probe scans across the sample in a raster pattern.

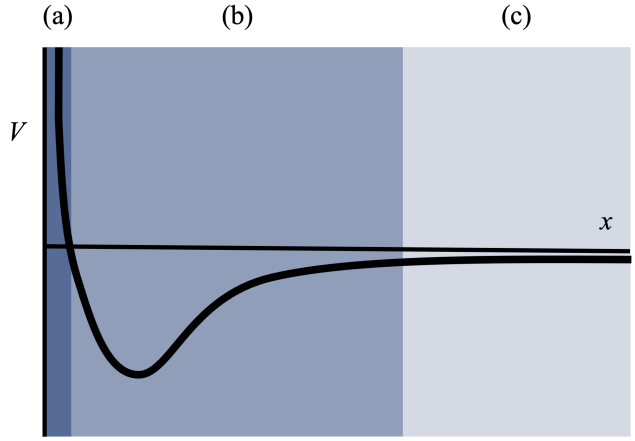

Figure 2.3: Lennard-Jones potential plot which describes the potential between the AFM tip and the sample surface. (a) At close distances the potential causes a repulsive force. (b) The potential causes an attractive force. (c) The potential tends to zero at larger distances.

The specific AFM used in this thesis was a Bruker Multimode 8 using PeakForce Tapping® mode and ScanAsyst® software. A colour camera and 10x objective are used to view the sample surface and align the location of the can-

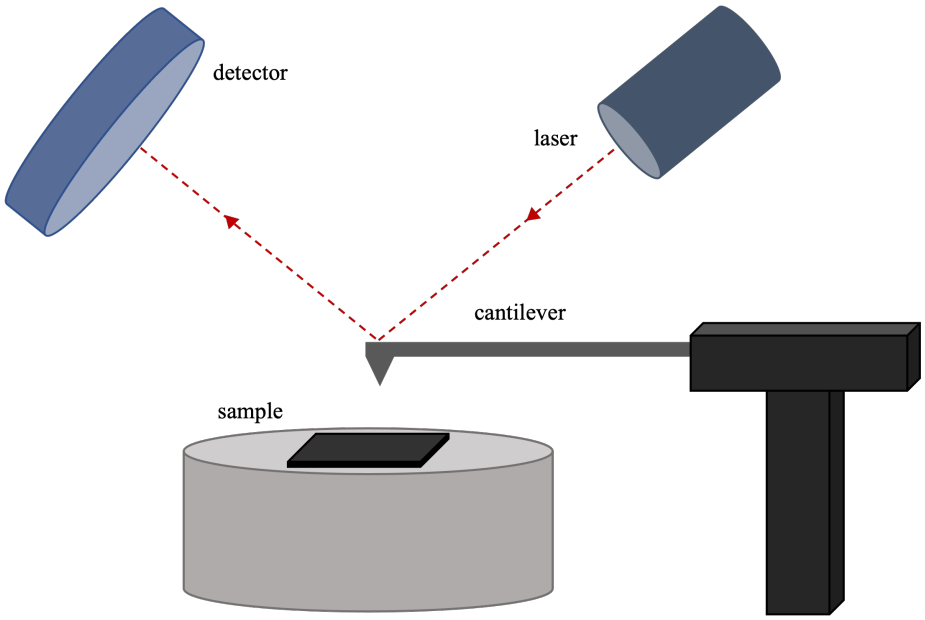

Figure 2.4: Schematic of the basic components of an AFM including the sample, cantilever, laser and detector.

tilever in regards to the surface.

For the experiments in this thesis, the stepped polymer samples were imaged with AFM prior to heating; then heated for 30 s, thermally quenched to halt any flow of the liquid polymers and scanned again. This process was completed several times at various time points up to 5 min. At each time point the AFM scan was completed in the exact same location on the sample.

Chapter 3

Results

In this chapter, I present the results associated with two different types of experiments. First, I examine the wrinkling phenomena associated with heating a bilayer film system: a PSU film atop a PS covered Si substrate. Due to thermal expansion and the flow of the PS film, once the sample is heated above the T_g value of PS, this sample wrinkles as discussed in sections 1.1.3 and 1.2.3. I explored this wrinkling to better understand the way in which I could eliminate this phenomenon for the remaining experiments. Next I give details for experiments involving a stepped trilayer film system: a PS covered Si wafer with a PSU film on top that is partially covered by another PS film. This stepped trilayer system is heated to a temperature at which the two PS films become liquids while the middle PSU film remains a glassy solid. This section is split into two parts: the first discusses the data analysis of the stepped AFM profiles. The second part examines the effects of the base liquid film height on the topology of the glassy PSU film floating at a liquid boundary.

3.1 Wrinkling Dynamics

When a thin glassy film is layered on top of a thin liquid film, the sample will wrinkle due to the compressive stress upon heating discussed in section 1.1.3. My system involves a glassy film of PSU and a liquid PS film. This wrinkling was investigated with the aim to eliminate this patterning to simplify further experiments. Optical microscopy videos were taken of samples as they wrinkled over the course of 20 min while heating to a temperature of 140 °C. Figure 3.1 shows an optical microscopy image of the wrinkled surface and the inset shows an AFM scan of the sinusoidal patterning of the sample surface.

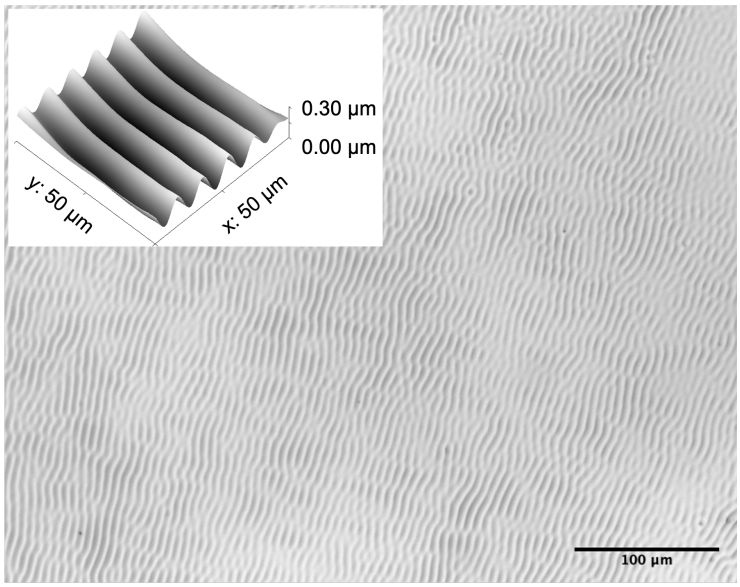

Figure 3.1: Optical microscopy image of a wrinkled sample where the greyscale intensity is the result of variations in the thickness of the sample. Inset shows an AFM scan of the wrinkled sample with wavelength, λ.

Wrinkling wavelength measurements were obtained by running the optical microscopy videos through a custom python code that takes a 2D Fourier transform of the image. A 2D Fourier transform is an image in frequency space that can help to identify periodicities in an image. The Fourier transform for the

image in Figure 3.1 show concentric rings aligned with the center of the image as shown in Figure 3.2. Figure 3.2 also shows the alignment of wrinkling shown by the anisotropic intensity of the rings. Calculating the radius of the smallest ring - which corresponds to the wrinkling wavelength of the sample gives the frequency and therefore the inverse of this radius is the wavelength, λ. A log-log plot of the wrinkling wavelength as a function of time in Figure 3.3 correspond to three identical samples prepared with a 470 $\pm$ 5 nm thick PS base film and a 168 $\pm$ 5 nm thick PSU film on top. The data sets analyzed agree with the $t^{1/6}$ power law expected by single-phase spreading theory [28] as shown by the slope of the black line on Figure 3.3. There is curvature at early times as the sample reaches thermal equilibrium during the heating from room temperature to 140 °C.

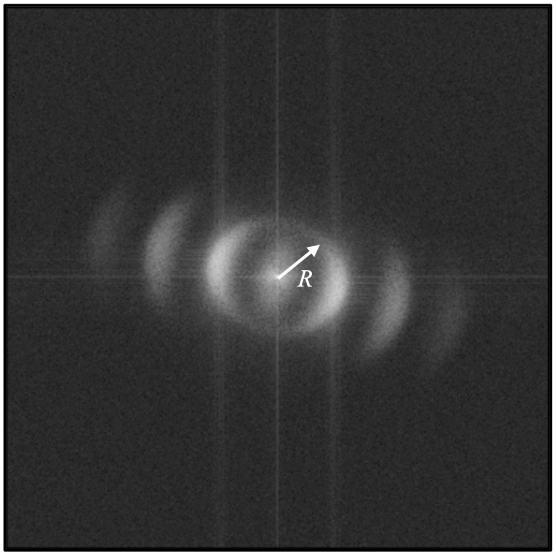

Figure 3.2: A characteristic 2D Fourier transform for wrinkling experiment sample. This image shows alignment of wrinkles as seen by the azimuthal anisotropy of the intensity of the rings. The radius, R, gives the frequency of the wrinkling patterns.

For the results in the next section, the samples were annealed above T_g of PSU to relax the films so that wrinkling phenomena is eliminated from the

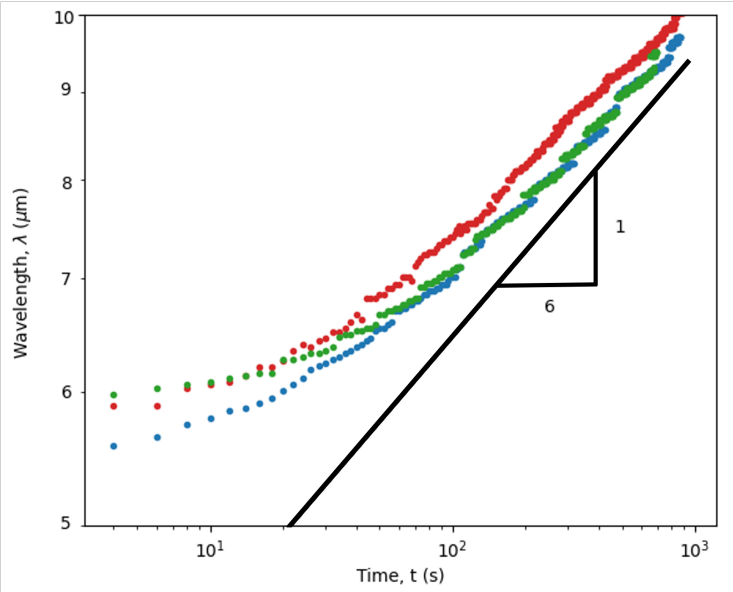

Figure 3.3: Double logarithmic plot of wrinkling wavelength as a function of time. Three data sets are plotted (red, green and blue circles) all having identical film thicknesses. The black line corresponds to the $t^{1/6}$ power law predicted by theory.

system. This annealing procedure ensures both films are liquids so they can flow and release all stresses associated with thermal expansion. The removal of wrinkling patterning simplifies the system to allow for analysis of the effects of the boundary condition only.

3.2 Data Analysis

Due to the length scales present in the system, specialized data analysis had to be developed to process the AFM data. The horizontal length scales in the samples were large enough such that the piezoelectric scanning in the AFM created background curvature. The step profiles obtained from the AFM were analyzed using a custom python code to background subtract artifacts before further analysis was done. The background subtraction involved averaging 20 -

30 lines of data that run perpendicular to the step to obtain a single profile of the step. This averaging process is shown in Figure 3.4 where a top down view of an AFM scan of a stepped sample is shown and a red box outlines the lines of data which were averaged. This averaging was done on only 20-30 lines to ensure the underlying background curvature was as similar as possible before the background was subtracted. Figure 3.5 shows the averaged profile (blue) for the AFM scan shown in Figure 3.4. A quartic function was fit to this profile and subsequently subtracted from the stepped profile to remove the background curvature. To fit the quartic function, the center region of the step was removed from the data set and the step height measured from the initial $t = 0$ s scan was entered into the minimization equation to obtain the fit parameters for the subsequent time points. The orange line in Figure 3.5 is the quartic function fit to the stepped profile. It should be noted that the aspect ratio of the profile in Figure 3.5 is large as the vertical scale is in nm while the horizontal scale is in µm.

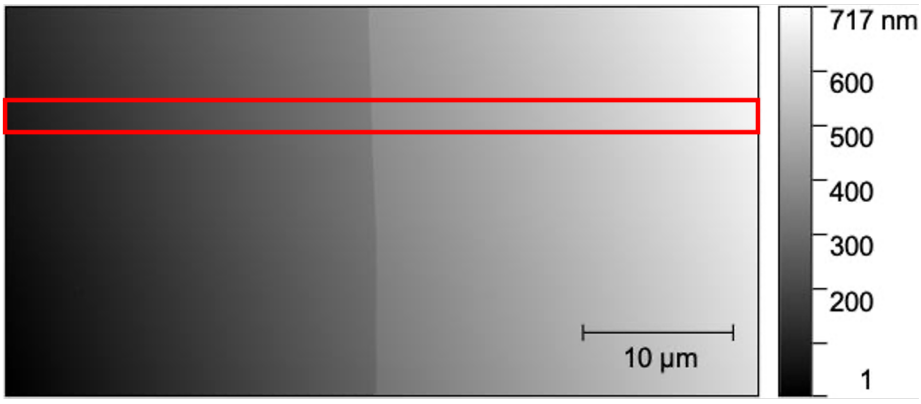

Figure 3.4: AFM image of a stepped sample with the step running vertically through the image. The red box shows the lines of data that were averaged to create a single profile for which further data analysis was done. Height is given by grey intensity scale on the right.

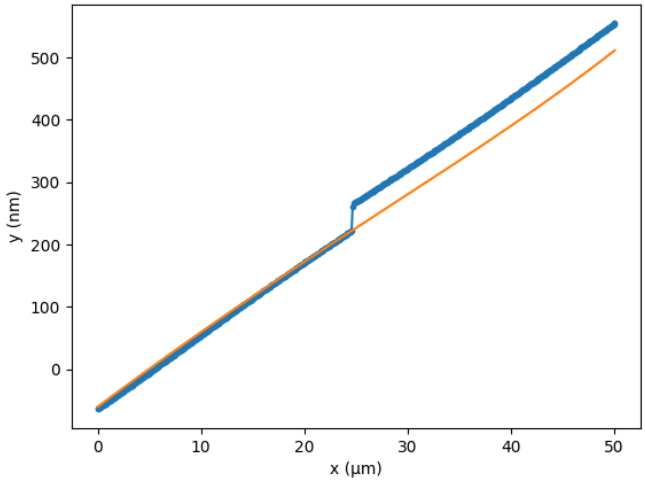

Figure 3.5: Averaged profile for AFM scan shown in Figure 3.4 (blue) with the corresponding background curvature function that is to be subtracted off (orange).

3.3 Capillary Forces Acting on a Solid Film

The effects of base film thickness on the topology of the step was investigated. Figure 3.6 shows a schematic of the sample geometry where the different films are labelled as h_1, h_2 and h_3 sequentially from the substrate upwards. Three stepped samples were analyzed at various time points ranging from 0 s to 300 s: $h_1 = 0$ nm (no h_1), $h_1 = 120 \pm 5$ nm and $h_1 = 493 \pm 5$ nm. Figure 3.7 shows a top down view of the $h_1 = 493$ nm sample at various time points where the material flow is seen by the widening and smoothing of the step over time. Figure 3.8 shows the times series for the stepped profiles associated with the $h_1 = 493$ nm thick sample. Figure 3.9 shows the times series for the stepped profiles associated with the no h_1 step sample. The quartic background curvature has been removed from both sets of profiles shown in Figures 3.8 and 3.9. Remaining curvature is present in both sets of data and will be handled in the next step of analysis.

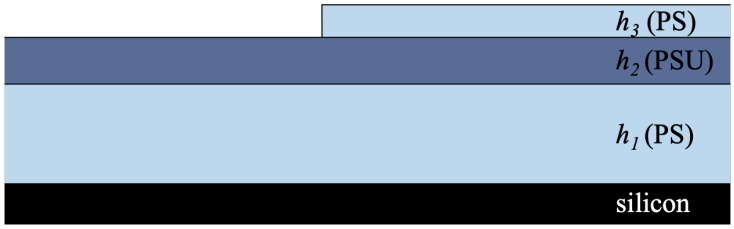

Figure 3.6: Schematic of the sample geometry with the films labelled with the thicknesses h_1, h_2 and h_3.

The bump seen in h_3 in Figures 3.8 and 3.9 for t = 30 s - 300 s, is a characteristic feature associated with capillary levelling of steps. This bump is usually seen in conjunction with a dip on the lower side of the step as capillary-driven flow levels the step [2, 30–32, 35]. In our system, the solid PSU film divides the base PS liquid from the PS liquid creating the step therefore flow between these levels cannot happen and the dip is not seen. Instead, the surface tension at the contact line of the liquid h_3 layer pulls up on the glassy h_2 film as described by γ_A in Figure 1.13. This surface tension force along with the constraint that the volume in h_3 must maintain a constant volume as it dewets from h_2, produces the accumulation of material in the bump in h_3. Due to the insertion of this glassy h_2 layer, we expect the dynamics of this system to be modified from that of previous work.

Once the background quartic function was subtracted from each profile, the initial profile at $t = 0$ s was subtracted from each subsequent time point for a given sample. The subtraction was done to eliminate any remaining curvature still present and to show only the differences with time. The assumption made for this $t = 0$ s subtraction is that the remaining curvature after the background subtraction is the same in each sample. The $h_1 = 493$ nm sample profiles for each time point after the $t = 0$ s subtraction are shown in Figure 3.10 where the aspect ratio is large since the horizontal dimension is three orders of magnitude greater than the vertical. As seen by the similarities in the curvature of the

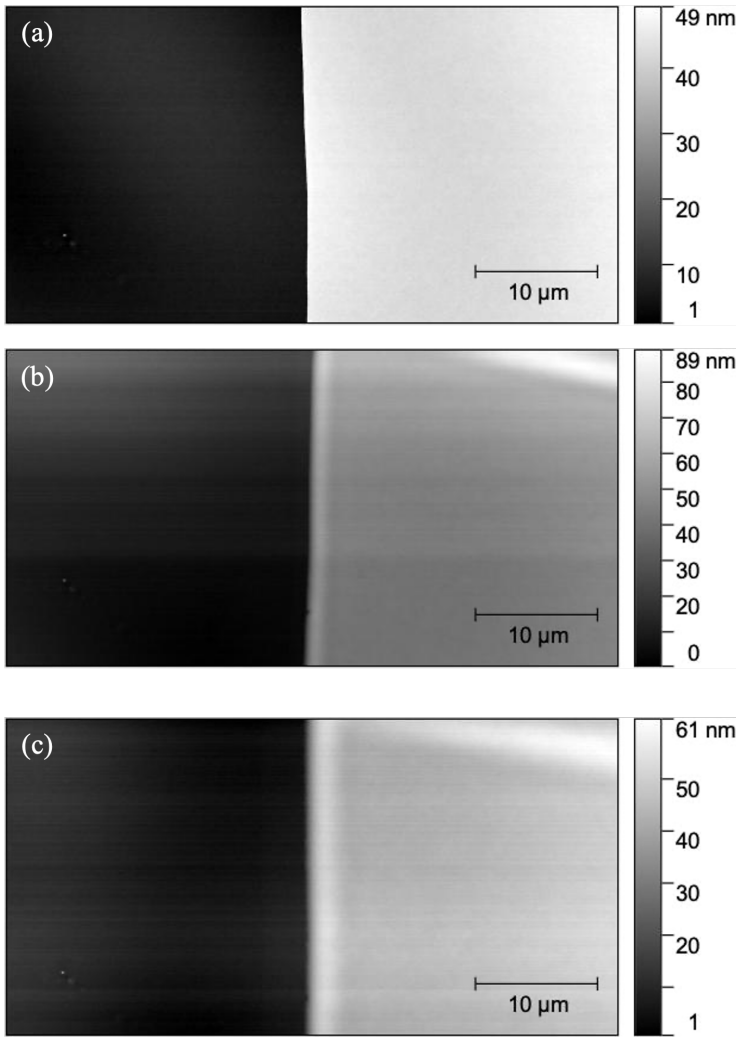

Figure 3.7: AFM time series showing the step for the $h_1 = 493$ nm sample. (a) $t = 0$ s time point. (b) $t = 30$ s time point. (c) $t = 300$ s time point. The edge of the step widens and smooths over time.

profiles in Figure 3.8, the assumption made for this $t = 0$ s subtraction is appropriate. We were interested in how these capillary levelling features change with time, and between samples with varying h_1 thicknesses. We wanted to better understand how surface tension forces at the h_3 contact line and Laplace

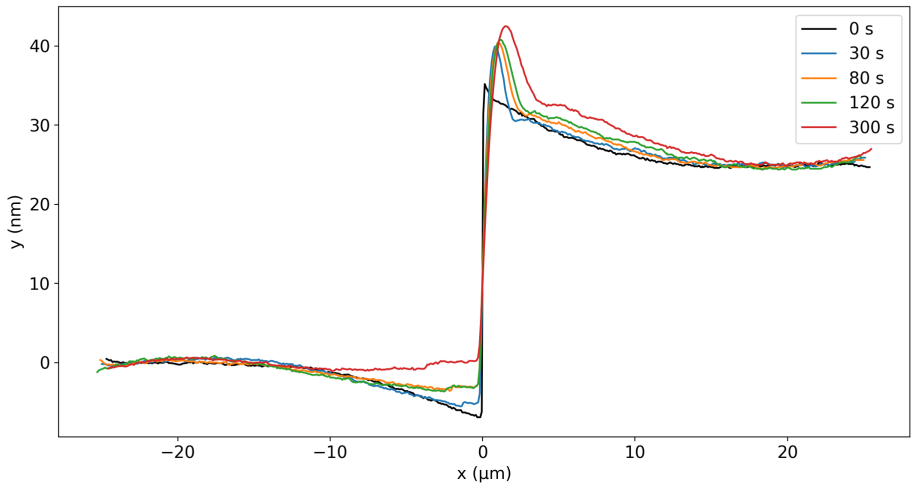

Figure 3.8: Profiles of $h_1 = 493$ nm sample after removing background curvature. Remaining curvature is still present in the samples.

pressure in the h_3 liquid affect the dynamical flow of the system.

Marked as Δx and Δy on Figure 3.10, a measurement of the horizontal and vertical scale are obtained for each time point for all three samples. The exact definitions of Δx and Δy were chosen because they correspond to characteristic features of the profiles present at all time points and in all samples ensuring reproducibility, and they were robust parameters which characterize the dynamics. Plots of Δx and Δy are shown in Figures 3.11 and 3.12.

The log-log plot in Figure 3.11 shows a linear trend. All three data sets, with varying h_1 thicknesses ranging from 0 nm to 493 nm are in good agreement with one another. As the h_3 film levels to reduce it's excess surface energy, we would expect differences in Δx between various h_1 thicknesses due to the viscous dissipation in the liquid h_1 layer. For example, a thicker liquid layer has more fluid material and may therefore have a better ability to dissipate the h_3 levelling, but unexpectedly, this is not seen in the results. The agreement between samples suggests the addition of the liquid h_1 layer does not affect the flow of fluid in the h_3 layer in the x-direction.

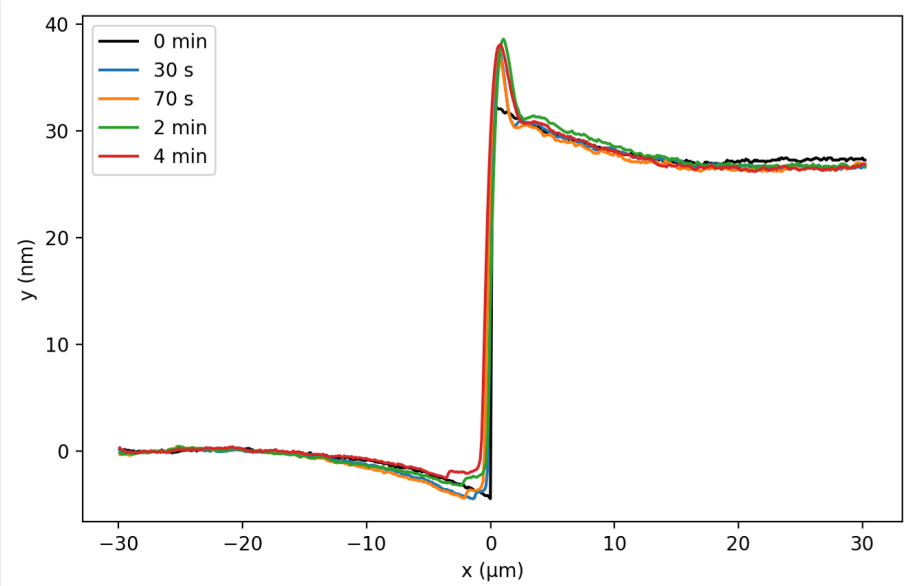

Figure 3.9: Profiles of the no h_1 sample after removing background curvature. Remaining curvature is still present in the samples and similar to the remaining curvature seen in the profiles in Figure 3.8.

The black line in Figure 3.11 shows a $t^{1/4}$ power law. A $t^{1/4}$ power law has been measured previously for the width growth of a liquid stepped polymer film [31]. In McGraw *et al.*, the stepped polymer film sat atop a solid Si substrate and our agreement with this power law suggests our h_2 film was too thick to allow for significant dissipation in the liquid h_1 film. A $t^{1/6}$ power law has been seen previously for an elastic substrate and is what we expected for this system [2]. Another reason for our unexpected agreement between samples is that our measurements did not span long enough times to allow for discrepancies between h_1 thicknesses to be seen which may only become significant at longer times.

In contrast to the lack of dependence on h_1 in Figure 3.11, the plot in Figure 3.12 which plots the Δy measurement, shows a difference between the case when $h_1 = 0$ and when $h_1 = 120$ nm and 493 nm. Specifically, when $h_1 = 0$, Δy is

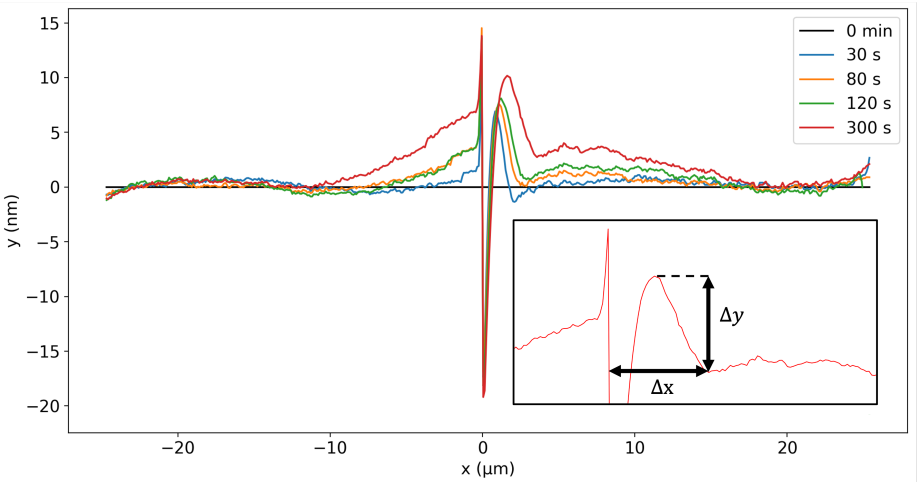

Figure 3.10: Profiles after $t = 0$ s subtraction for $h_1 = 493$ nm thick PS base sample. Inset shows the zoomed in center region of the $t = 300$ s profile with Δx and Δy labelled.

larger than when measured for the cases when $h_1 \neq 0$. This is understood by the solid PSU film bending due to forces acting on it while the PSU film does not have the ability to flex out of the lateral plane when $h_1 = 0$. Specifically, curvature introduced by the capillary levelling of the step means that there is a Laplace pressure difference inside the liquid versus outside this liquid. Shown in Equation 1.20, the pressure difference is given by the product of the curvature and surface tension. For deformations above the initial height, the radii of curvature point into the liquid and for deformations below the initial height, the radii of curvature point out of the liquid which results in a positive Laplace pressure at the bump, and a negative Laplace pressure at the dip. The pressure at different locations within the sample are shown in Figure 3.13(a). When the Laplace pressure force acts down on the underlying PSU film the film bends downward to accommodate this stress. The consequence of the Laplace forces is that the bump features seen in the topology of the step are dampened as the results show in Figure 3.12. A schematic of the Laplace pressure effects on the h_2 film are shown in Figure 3.13(b).

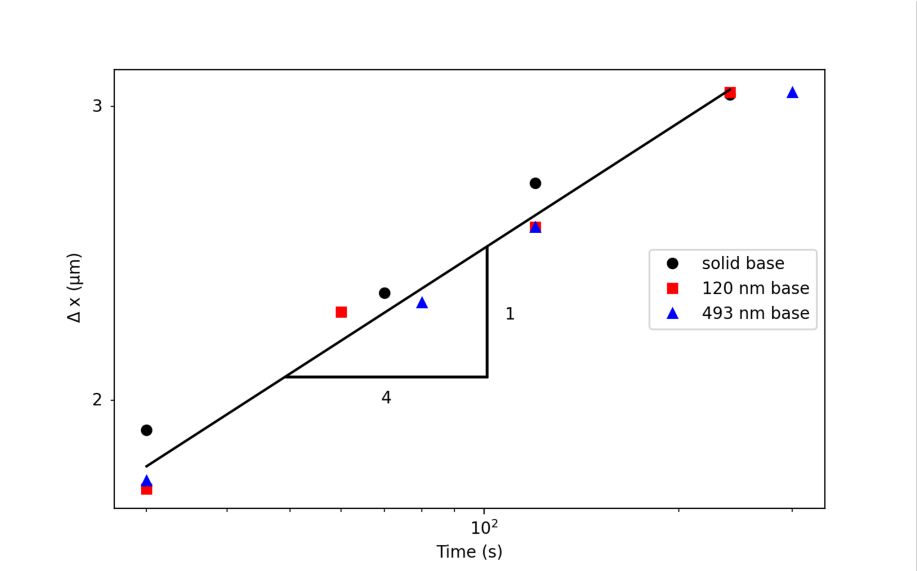

Figure 3.11: Log-log plot of Δx as a function of time for three data sets corresponding to $h_1 = 0$ nm (black circles), $h_1 = 120$ nm (red squares) and $h_1 = 493$ nm (blue triangles). The black line corresponds to a $t^{1/4}$ power law.

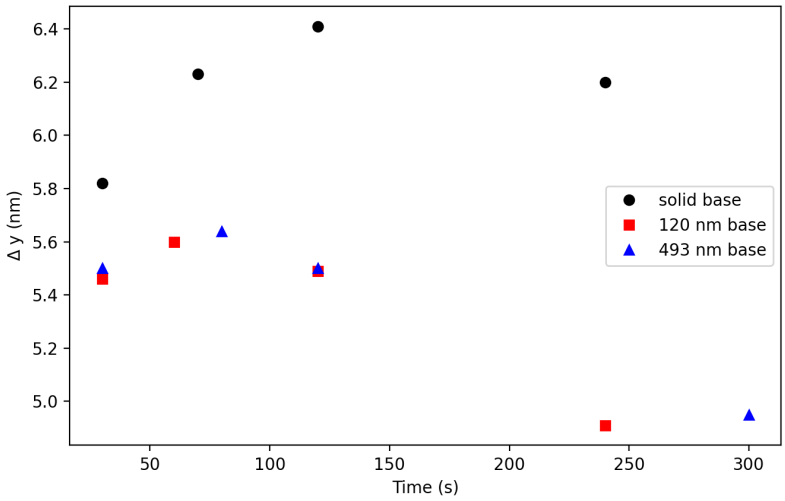

Figure 3.12: Plot of Δy as a function of time for three data sets corresponding to $h_1 = 0$ nm (black circles), $h_1 = 120$ nm (red squares) and $h_1 = 493$ nm (blue triangles).

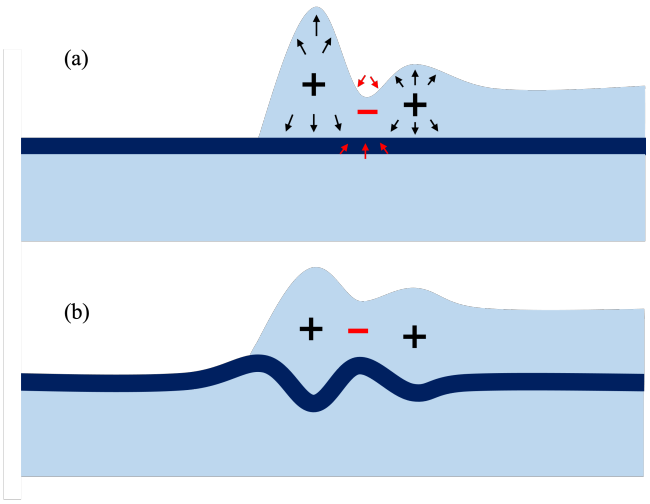

Figure 3.13: Schematic of the final samples after capillary driven flow has begun to level step. (a) Fluid step with red arrows describing the forces associated with the Laplace pressure acting on the dark blue pliable PSU film. (b) Bent PSU film due to the Laplace pressures showing the vertical decrease in step height.

Chapter 4

Conclusions

Thin polymer films were used as an ideal system to analyze the effects of a liquid boundary on a floating pliable solid film. A trilayer sample was created so that when heated to 150 °C the bottom and top film become liquids while the middle layer remains a glassy solid. The top liquid film partially covers the underlayers acting as a stepped liquid boundary we were interested in investigating. The thickness of the base liquid film was varied. We found that the expected capillary levelling bump explored in previous work [2, 30–32, 35] was also seen in our system. Results suggested the liquid film base did not play a significant role in the flow dynamics along the x-direction but did affect the vertical scale of the bump. We understand this result in terms of the Laplace pressure forces acting up or down on the pliable intermediate sheet depending on the curvature associated with the bump. The glassy sheet is thin enough that it bends to accommodate these pressure forces which alter the vertical scale of profile.

This trilayer system could be further used to investigate the effects of solid film rigidity on the flow dynamics as well as dewetting rates of the liquid step. We also hope to analyze the solid film deformations on the low side of the step with this stacked thin film geometry.

Bibliography

[1] Pierre-Gilles de Gennes, Françoise Brochard-Wyart, and David Quéré. *Capillarity and Wetting Phenomena Drops, Bubbles, Pearls, Waves*. Springer-Verlag, 2004.

[2] Marco Rivetti, Vincent Bertin, Thomas Salez, Chung-Yuen Hui, Christine Linne, Maxence Arutkin, Haibin Wu, Elie Raphaël, and Oliver Bäumchen. Elastocapillary levelling of thin viscous films on soft substrates. *Physical Review Fluids*, 2:094001, 2017.

[3] William B. Liechty, David R. Kryscio, Brandon V. Slaughter, and Nicholas A. Peppas. Polymers for drug delivery systems. *Annual Review of Chemical and Biomolecular Engineering*, page 149, 2010.

[4] Alexander Oron, Stephen H. Davis, and S. George Bankhoff. Long-scale evolution of thin liquid films. *Reviews of Modern Physics*, 69(3):931–980, July 1997.

[5] J.T. Koberstein. Polymer surfaces and interfaces. *MRS Bulletin*, pages 16–18, 1996.

[6] John R. Dutcher, Kari Dalnoki-Veress, Bernie G. Nickel, and Connie B. Roth. Instabilities in thin polymer films: From pattern formation to rupture. *Macromolecular Symposia*, 159:143–150, 2000.

[7] Thomas P. Russell and Yu Chai. 50th anniversary perspective: Putting the squeeze on polymers: A perspective on polymer thin films and interfaces. *Macromolecules*, 50:4597–4609, 2017.

[8] Michael Rubinstein and Ralph H. Colby. *Polymer Physics*. Oxford University Press, 2003.

[9] J. Brandrup, E. H. Immergut, and E. A. Grulke. *Polymer Handbook*. John Wiley & Sons, Inc, 4 edition, 1999.

[10] R. A. L. Jones. *Soft Condensed Matter*. Oxford University Press, 2002.

[11] Mary Anne White. *Physical Properties of Materials*. CRC Press, second edition, 2012.

[12] Daniel V. Schroeder. *An Introduction to Thermal Physics*. Addison Wesley Longman, 2000.

[13] Cun Feng Fan and Shaw Ling Hsu. Application of the molecular simulation technique to characterize the strutcure and properties of an aromatic polysulfone system. *Macromolecules*, 25:266–270, 1992.

[14] Yasumasa Okada and Yozo Tokumaru. Precise determination of lattive parameter and thermal expansion coefficient of silicon between 200 and 1500 k. *Journal of Applied Physics*, 56(2):314–320, July 1984.

[15] Edwin P. Chan and Alfred J. Crosby. Spontaneous formation of stable aligned wrinkling patterns. *Soft Matter*, 2:324–328, 2006.

[16] Edwin P. Chan and Alfred J. Crosby. Fabricating microlens arrays by surface wrinkling. *Advanced Materials*, 18:3238–3242, 2006.

[17] Derek Breid and Alfred J. Crosby. Effect of stress state on wrinkle morphology. *Soft Matter*, 7:4490–4496, 2011.

[18] A. L. Volynskii, S. Bazhenov, O. V. Lebedeva, and N. F. Bakeev. Mechanical buckling instability of thin coatings deposited of soft polymer substrates. *Journal of Materials Science*, 35:547–554, 2000.

[19] Christopher M. Stafford, Christopher Harrison, Kathryn L. Beers, Alamgir Karim, Eric J. Amis, Mark R. Vanlandingham, Ho-Cheol Kim, Willi Volksen, Robert D. Miller, and Eva E. Simonyi. A buckling-based metrology for measuring the elastic moduli of polymeric thin films. *Nature Materials*, 3:545–550, 2004.

[20] Krill Ekimenko, Mindaugas Rackaitis, L. Mahadevan Evangelos Manias nad Ashkan Vazir, and Jan Genzer. Nested self-similar wrinkling patterns in skins. *Nature Materials*, 4:293–297, 2005.

[21] Pei-Chun Lin and Shu Yang. Spontaneous formation of one-dimensional ripples in transit to highly ordered two-dimensional herringbone structures through sequential and unequal biaxial mechanical stretching. *Applied Physics Letters*, 90:241903, 2007.

[22] John F. Niven, Gurkaran Chowdhry, James S. Sharp, and Kari Dalnoki-Veress. The emergence of local wrinkling or global buckling in thin free-standing bilayer films. *The European Physical Journal E*, 43:20, 2020.

[23] Yuri Ebata, Andrew B. Croll, and Alfred J. Crosby. Wrinkling and strain localizations on polymer thin films. *Soft Matter*, 8:9086–9091, 2012.

[24] Ned Bowden, Scott Brittain, Anthony G. Evans, John W. Hutchinson, and George M. Whitesides. Spontaneous formation of ordered structures in thin films of metals supported on an elastomeric polymer. *Nature*, 393:146–149, 1998.

[25] D. J. Acheson. *Elementary Fluid Dynamics*. Oxford Univeristy Press Inc., 1990.

[26] L. D. Landau and E. M. Lifshitz. *Theory of Elasticity*. Pergamon Press, 1970.

[27] A. E. Hosoi and L. Mahadevan. Peeling, healing and bursting in a lubricated elastic sheet. *Physical Review Letters*, 93(13):137802, September 2004.

[28] Talal T. Al-Housseiny, Ivan C. Christov, and Howard A. Stone. Two-phase fluid displacement and interfacial instabilities under elastic membranes. *Physical Review Letters*, 111(3):034502, 2013.

[29] Thomas Salez, Joshua D. McGraw, Sara L. Cormier, Oliver Bäumchen, Kari Dalnoki-Veress, and Elie Raphaël. Numerical solution of thin film equations for polymer flows. *European Physical Journal E*, 35:1–9, 2012.

[30] Joshua D. McGraw, Thomas Salez, Oliver Bäumchen, Elie Raphaël, and Kari Dalnoki-Veress. Self-similarity and energy dissipation in stepped polymer films. *Physical Review Letters*, 109:128303, 2012.

[31] Joshua D. McGraw, Nicholas M. Jago, and Kari Dalnoki-Veress. Capillary levelling as a probe of thin film polymer rheology. *Soft Matter*, 7:7832–7838, 2011.

[32] Matilda Backholm, Michael Benzaquen, Thomas Salez, Elie Raphaël, and Kari Dalnoki-Veress. Capillary levelling of a cylindrical hole in a viscous film. *Soft Matter*, 10:2550–2558, 2014.

[33] Michael Benzaquen, Paul Fowler, Laetitia Jubin, Thomas Salez, Kari Dalnoki-Veress, and Elie Raphaël. Approach to universal self-similar attractor for the levelling of thin liquid films. *Soft Matter*, 10:8608–8614, 2014.

[34] Oliver Bäumchen, Michael Benzaquen, Thomas Salez, Joshua D. McGraw, Matilda Backholm, Paul Fowler, Elie Raphaël, and Kari Dalnoki-Veress. Relaxation and intermediate asymptotics of a rectangular trench in a viscous film. *Physical Review E*, 88:035001, 2013.

[35] Joshua D. McGraw, Thomas Salez, Oliver Bäumchen, Elie Raphaël, and Kari Dalnoki-Veress. Capillary levelling of stepped films with inhomogenous molecular mobility. *Soft Matter*, 9:8297–8305, 2013.

[36] Mark Ilton, Miles M. P. Couchman, Cedric Gerbelot, Michael Benzaquen, Paul D. Fowler, Howard A. Stone, Elie Raphaël, Kari Dalnoki-Veress, and Thomas Salez. Capillary levelling of free-standing liquid nanofilms. *Physical Review Letters*, 117:167801, 2016.

[37] L.E. Stillwagon and R. G. Larson. Fundamentals of topographic substrate leveling. *Journal of Applied Physics*, 63(11):5251–5258, June 1988.

[38] R. W. Collins. Automatic rotating element ellipsometers: Calibration, operation, and real-time applications. *Review of Science Instruments*, 61:2029–2062, 1990.